Original Article

Artificial intelligence-measured nodule mass for determining the invasiveness of neoplastic ground glass nodules

Ting-Wei Xiong[1,2#], Hui Gan[1,2#], Fa-Jin Lv[1], Xiao-Chuan Zhang[3], Bin-Jie Fu[1^], Zhi-Gang Chu[1^]

[1]Department of Radiology, The First Affiliated Hospital of Chongqing Medical University, Chongqing, China; [2]Department of Radiology, The Second Affiliated Hospital of Army Medical University, Chongqing, China; [3]Department of Radiology, Chonggang General Hospital, Chongqing, China

Contributions: (I) Conception and design: BJ Fu, ZG Chu; (II) Administrative support: ZG Chu, FJ Lv; (III) Provision of study materials or patients: ZG Chu, FJ Lv, BJ Fu; (IV) Collection and assembly of data: TW Xiong, H Gan, XC Zhang; (V) Data analysis and interpretation: TW Xiong, XC Zhang; (VI) Manuscript writing: All authors; (VII) Final approval of manuscript: All authors.

[#]These authors contributed equally to this work.

Correspondence to: Bin-Jie Fu, MD; Zhi-Gang Chu, MD, PhD. Department of Radiology, The First Affiliated Hospital of Chongqing Medical University, No. 1 Youyi Road, Yuanjiagang, Yuzhong District, Chongqing 400016, China. Email: binjie_fu@163.com; chuzg0815@163.com.

Background: The nodule mass is an important indicator for evaluating the invasiveness of neoplastic ground-glass nodules (GGNs); however, the efficacy of nodule mass acquired by artificial intelligence (AI) has not been validated. This study thus aimed to determine the efficacy of nodule mass measured by AI in predicting the invasiveness of neoplastic GGNs.

Methods: From May 2019 to September 2023, a retrospective study was conducted on 755 consecutive patients comprising 788 pathologically confirmed neoplastic GGNs, among which 259 were adenocarcinoma in situ (AIS), 282 minimally invasive adenocarcinoma (MIA), and 247 invasive adenocarcinoma (IAC). Nodule mass was quantified using AI software, and other computed tomography (CT) features were concurrently evaluated. Clinical data and CT features were compared using the Kruskal-Wallis test or Pearson chi-square test. The predictive efficacy of mass and CT features for evaluating invasive lesions (ILs) (MIAs and IACs) and IACs was analyzed and compared via receiver operating characteristic (ROC) analysis and the Delong test.

Results: ROC curve analysis revealed that the optimal cutoff value of mass for distinguishing ILs and AISs was 225.25 mg [area under the curve (AUC) 0.821; 95% confidence interval 0.792–0.847; sensitivity 64.27%; specificity 89.19%; P<0.001], and for differentiating IACs from AISs and MIAs, it was 390.4 mg (AUC 0.883; 95% confidence interval 0.858–0.904; sensitivity 80.57%; specificity 86.32%; P<0.001). The efficacy of nodule mass in distinguishing ILs and AISs was comparable to that of size (P=0.2162) and significantly superior to other CT features (each P value <0.001). Additionally, the ability of nodule mass to differentiate IACs from AISs and MIAs was significantly better than that of CT features (each P value <0.001).

Conclusions: AI-based nodule mass analysis is an effective indicator for determining the invasiveness of neoplastic GGNs.

Keywords: Artificial intelligence (AI); adenocarcinoma; nodule; nodule mass; invasiveness

Submitted Mar 31, 2024. Accepted for publication Aug 12, 2024. Published online Aug 28, 2024.
doi: 10.21037/qims-24-665
View this article at: https://dx.doi.org/10.21037/qims-24-665

^ ORCID: Bin-Jie Fu, 0000-0002-6863-2827; Zhi-Gang Chu, 0000-0002-2441-8132.

Introduction

With the widespread application of low-dose computed tomography (LDCT) in lung cancer screening, the detection rate of ground-glass nodules (GGNs) has significantly increased. On computed tomography (CT) images, GGNs appear as pure ground-glass nodules (pGGNs) or part-solid nodules (PSNs) based on their density (1). Pathologically, they can generally be classified as neoplastic or nonneoplastic. Among neoplastic GGNs, pGGNs are typically associated with adenocarcinoma in situ (AIS) and less commonly minimally invasive adenocarcinoma (MIA) or invasive adenocarcinomas (IAC); meanwhile, PSNs are more likely to be MIA or IAC (2,3). The pathological type of neoplastic GGNs considerably influences the subsequent treatment and prognosis.

At present, surgical resection remains the preferred treatment for neoplastic GGNs in clinical practice. The details of surgical management vary depending on the degree of invasiveness. Limited resections such as wedge resection and segmental resection are suitable for AIS and MIA, while lobectomy is recommended for IAC (4). Additionally, the risk of lymph node metastasis and prognosis varies across different subtypes. Studies indicate that local lymph node metastasis mostly occurs in MIA and IAC and that IAC requires lymph nodule dissection (5-7). The 5-year disease-free survival rate after complete resection of AIS and MIA is 100%, whereas the 5-year survival rate after complete resection of IAC is 70–90% (3,8). Therefore, accurately evaluating the invasiveness of GGNs before operation is crucial.

Previous studies have introduced various methods to assess the invasiveness of neoplastic GGNs, including axial long diameter (AXLD), mean density, CT-based morphological features, the invasion of lung adenocarcinoma by GGN features (ILAG) predictive models, semiautomatic segmentation, and others (2,9-11). de Hoop *et al.* were first to report that the presence of a mass can indicate the growth of GGNs earlier than can changes in diameter and volume (12). The mass can be used to evaluate the change of GGNs more accurately, objectively, and comprehensively and to reflect the size and internal attenuation of GGN simultaneously. Furthermore, the nodule mass has been shown to be a reliable independent risk factor for distinguishing subtypes of neoplastic GGNs, and an optimal cutoff of mass could be used for differentiating IACs from MIAs or AISs (13). Therefore, the nodule mass may be an important predictive indicator of the invasiveness of GGNs.

Nodule mass can be derived through a formula based on the semiautomatic segmentation of diameter or volume (14,15). However, this method is time-consuming, inconvenient, and prone to measurement errors due to the ill-defined boundaries of GGNs and difficulties in standardizing manual measurements. With the development of computer technology, artificial intelligence (AI) software has become increasingly popular. Nodule net, principal component analysis (PCA), training datasets, machine learning (ML) [including support vector machine (SVM) and random forest (RF)], deep learning (DL), convolutional neural network (CNN) [including three-dimensional unit network (3D U-Net), dense V-network (DenseV-Net), region pulmonary lobe segmentation network (RPLS-Net), and no-new-unit-Net (nnU-Net)], and a computer-aided detection (CADe) system have all been implemented in nodule segmentation, feature extraction and selection, and classification. These methods can characterize nodule morphology (e.g., boundary and spiculation), volume and volume doubling time, intensity, texture, heterogeneity, and peritumor features; quantify nodule features; and help differentiate between malignant and benign nodules (16-20). AI also offers a more stable and efficient method for obtaining nodule mass.

However, no studies on whether AI-based mass measurements can be used to differentiate between subtypes of neoplastic GGNs have been conducted thus far. The aim of this study was thus to assess the effectiveness of using AI-measured nodule mass in predicting the subtypes of neoplastic GGNs. We present this article in accordance with the STARD reporting checklist (available at https://qims.amegroups.com/article/view/10.21037/qims-24-665/rc).

Methods

The study was performed in accordance with the Declaration of Helsinki (as revised in 2013) and was approved by the Ethics Committee of The First Affiliated Hospital of Chongqing Medical University (No. 2019-062). The requirement for individual consent was waived due to the retrospective nature of the analysis.

Patients

From May 2019 to September 2023, patients with GGNs who underwent surgical resection in The First Affiliated Hospital of Chongqing Medical University were recruited for this study. The inclusion criteria were as follows: (I) a

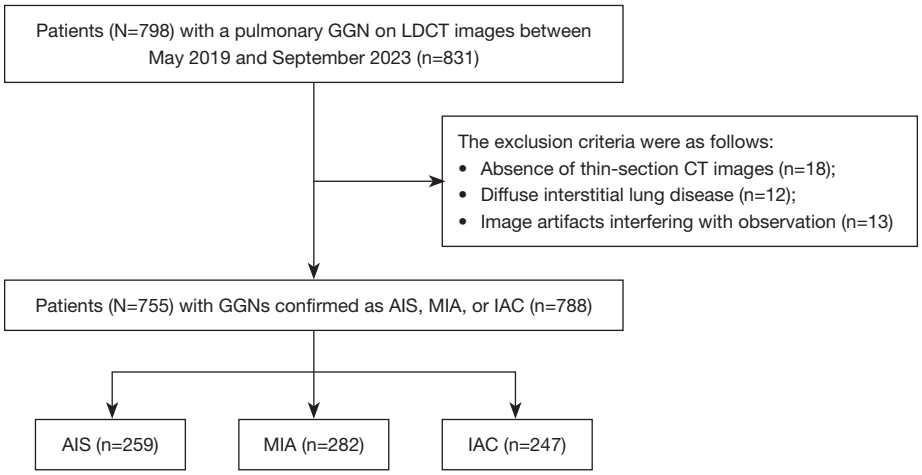

Figure 1 Flow diagram for the inclusion and exclusion of patients. GGN, ground-glass nodule; LDCT, low-dose computed tomography; CT, computed tomography; AIS, adenocarcinoma in situ; MIA, minimally invasive adenocarcinoma; IAC, invasive adenocarcinoma.

GGN diameter less than 3 cm; (II) availability of complete clinical and pathological data; (III) confirmation of GGNs as being AIS, MIA, or IAC through pathological examination; (IV) interval between surgery and CT examination less than 1 month; and (V) all examinations conducted by the same brand of CT scanner. Meanwhile, the exclusion criteria were as follows: (I) absence of thin-section CT images with a thickness of ≤1 mm, (II) presence of concomitant diffuse interstitial lung disease, and (III) severe artifacts or noise affecting image assessment. Among the initially screened patients, 18 were excluded due to the absence of thin-section CT images, 12 due to diffuse interstitial lung disease, and 13 due image artifacts interfering with observation. Ultimately, a total of 755 patients comprising 788 GGNs (259 AISs, 282 MIAs, and 247 IACs) were included in the analysis. The patient selection process is illustrated in *Figure 1*.

CT examination

The CT scans were conducted using the following scanners: SOMATOM Definition Flash, SOMATOM Perspective, and SOMATOM Force (Siemens Healthineers, Erlangen, Germany). Patients were instructed to perform a breath-hold maneuver before image acquisition. Scans were acquired from the thoracic inlet to the costophrenic angle at the end of inspiration during a single breath-hold, with the patient in a supine position. The data used in this study were acquired from CT scans performed under routine parameters rather from an LDCT scan. The CT images were obtained under the following parameters: tube voltage, 120–130 kVp; reference tube current, 50–140 mAs (with automatic current modulation technology); scanning slice thickness, 5 mm; rotation time, 0.5 seconds; pitch, 1.0–1.1; collimation, 0.60 mm; and matrix, 512×512. The images were reconstructed at a slice thickness and interval of 1.00 mm using a medium-sharpness algorithm.

Image acquisition and analysis

The patients' CT data were evaluated on a picture archiving and communication system (PACS) workstation (Vue PACS, Carestream, Rochester, NY, USA). Image analysis was mainly based on axial images with lung window settings [window level, −600 Hounsfield unit (HU); window width: 1,500 HU], with multiplanar reconstruction (MPR) images being used as a supplement. The CT features of GGNs were reviewed by two radiologists (T.W.X. and H.G., with more than 10 years of working experience), who were blinded to the clinical and pathological information. In cases of discordant opinions between the radiologists, consensus was reached through discussion.

The following indicators of GGNs were evaluated: (I) location, including right upper lobe, right middle lobe, right lower lobe, left upper lobe, and left lower lobe; (II) size, calculated as mean value of the longest diameter and the perpendicular diameter on axial CT images; (III) margin, including smooth or coarse; (IV) shape, including irregular or regular (round or oval); (V) boundary, including well-defined or ill-defined; (VI) lobulation, including a

wavy or scalloped configuration of the nodule's surface (4); (VII) spiculation, including long or short linear strands of the nodule surface (21); (VIII) vacuole sign, including round or irregular air attenuation within the nodule (11); (IX) air bronchial sign, including visible air-filled bronchi within the nodule); (X) internal vessel change, including dilation and distortion; and (XI) pleural indentation, including a linear shadow on the nodule surface pull on the pleura (22). Additionally, a lung nodule AI-assisted diagnosis system (InferRead CT Lung, InferVision Medical Health, Beijing, China) was used to automatically recognize and segment the GGNs from images and to subsequently obtain the nodule mass. The workflow for acquiring the nodule mass was as follows: step 1, the AI software automatically crawled thin-section chest CT images from PACS and detected all nodules; step 2, the AI software was used to find the target GGNs in the list; step 3, AI delineation of GGN boundaries in all sections was checked; step 4, the density histogram and other quantitative indicators of GGN were obtained through the nodule analysis module (*Figure 2*).

The pulmonary nodule AI-assisted diagnosis system was coupled with a DL algorithm to accomplish automatic segmentation of the boundary of GGNs. In the calculation process, the system automatically segments the GGNs and computes the number of voxels corresponding to each CT value in the whole lesion. Each CT value and the corresponding number of voxels are stored as a "list", and the "list" of the whole nodule is stored as a "dictionary". The information obtained is used for calculating the required index via the corresponding formula. The nodule mass was calculated based on the voxel method and the corresponding formula as follows: Mass = [nodule volume × (mean density + 1,000)]/1,000 (13,23).

Statistical analysis

All data were processed with SPSS 25 (IBM Corp., Armonk, NY, USA) and MedCalc (MedCalc Software, Ostend, Belgium) software. Clinical data and various CT features were statistically analyzed for each patient. A normality test was performed for continuous variables, which are expressed as the mean ± standard deviation (SD). Meanwhile, categorical variables are expressed as the frequency and percentage. The Kruskal-Wallis test was used for analyzing age and size, whereas the Pearson chi-square test was used for analyzing sex, shape, location, boundary, lobulation, spiculation, vacuole sign, air bronchial, vessel change, and pleural indentation. Subsequently, the optimal mass and size thresholds for determining ILs and IACs among the neoplastic GGNs were determined via receiver operating characteristic (ROC) analysis. The Delong test was used to compare the predictive performance of mass and that of other clinical and CT features. A P value (bilateral) less than 0.05 was considered statistically significant.

Results

Patients' clinical characteristics

The patients' clinical characteristics and CT features of GGNs are summarized in *Table 1*. The group with AIS had a greater proportion of females than did the group with IAC (P=0.008). Compared to the groups with AIS and MIA, the IAC group had a significantly higher patient age, nodule size, and mass (each P value <0.001). Compared with IACs, AISs and MIAs were likely to have a regular shape (P<0.001). Vacuole sign, vascular change, lobulation, spiculation, air bronchogram, and pleural indentation were more commonly detected in IACs than in MIAs and AISs (each P value <0.05).

Quantitative and qualitative indicators for predicting ILs and IACs

The quantitative and qualitative indicators for predicting ILs and IACs are shown in *Tables 2,3* and *Figure 3*. Among the indicators, the efficacy of nodule mass in differentiating between ILs and AISs and between IACs and MIAs/AISs was the highest and was followed by nodule size. The optimal cutoff value of mass for distinguishing ILs from AISs was 225.25 mg, while that for distinguishing IACs from AISs/MIAs was 390.4 mg. Regarding the GGNs in different lobes, the cutoff values of nodule mass for determining ILs and IACs are shown in *Tables 4,5*. According to the results, the cutoff values of nodule mass in the upper lobes and lower lobes for determining ILs (229.165 *vs.* 217.215 mg) and IACs (325.955 *vs.* 335.18 mg) were similar. Meanwhile, the optimal cutoff value of size for distinguishing ILs and AISs was 9.95 mm, while that for distinguishing IACs from AISs and MIAs was 10.9 mm. The efficacy of mass in distinguishing ILs and AISs was comparable to that of size (P=0.2162) and was significantly superior to other CT features (each P value <0.001). Additionally, the ability of nodule mass to differentiate IACs from AISs/MIAs was significantly better than that of size and other CT features (each P value <0.001) (*Figure 4*).

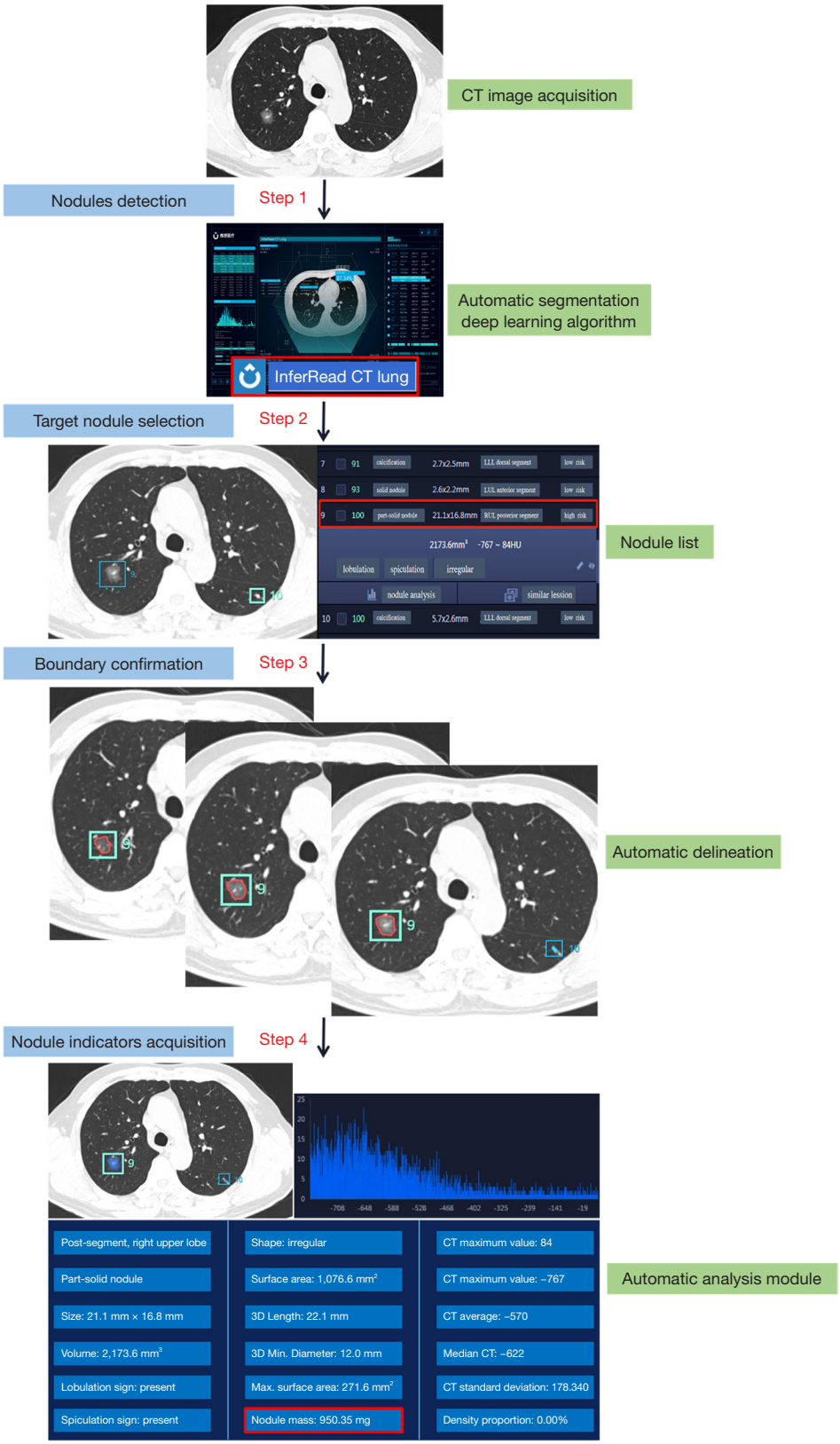

Figure 2 A schematic figure for the process of nodule mass acquisition. CT, computed tomography; 3D, three-dimensional.

Table 1 Clinical data and CT features of the patients with AIS, MIA, or IAC

Characteristic	Patients with AIS (n=259)[a]	Patients with MIA (n=282)[b]	Patients with IAC (n=247)[c]	P value
Number of patients	N=239	N=273	N=243	
Sex				0.008[e]
Male	56 (23.4)	79 (28.9)	84 (34.6)	
Female	183 (76.6)	194 (71.1)	159 (65.4)	
Age (years)	51.9±11.5	54.9±12.2	58.8±10.0	<0.001[f]
Size (mm)	8.0±2.8	10.4±4.0	15.5±5.0	<0.001[f]
Mass (mg)	139.7±232.7	355.1±490.9	1,446.3±2,003.1	<0.001[f]
CT pattern				<0.001[f]
Distribution				0.221
Upper lobe	173 (66.8)	174 (61.7)	167 (67.6)	
Middle lobe	14 (5.4)	27 (9.6)	13 (5.3)	
Lower lobe	72 (27.8)	81 (28.7)	67 (27.1)	
Shape				<0.001[f]
Regular	197 (76.1)	167 (59.2)	90 (36.4)	
Irregular	62 (23.9)	115 (40.8)	157 (63.6)	
Boundary				0.742
Ill-defined	21 (8.1)	20 (7.1)	22 (8.9)	
Well-defined	238 (91.9)	262 (92.9)	225 (91.1)	
Lobulation	20 (7.7)	53 (18.8)	104 (42.1)	<0.001[f]
Spiculation	10 (3.9)	36 (12.8)	85 (34.4)	<0.001[f]
Vacuole sign	20 (7.7)	31 (11.0)	41 (16.6)	0.007[e]
Air bronchogram	13 (5.0)	35 (12.4)	89 (36.0)	<0.001[f]
Vascular change	14 (5.4)	18 (6.4)	33 (13.4)	0.002[de]
Pleural indentation	17 (6.6)	32 (11.3)	63 (25.5)	<0.001[de]

Data are presented as the mean ± standard deviation or N (%). There were significant differences between groups a and b, a and c, and b and c for age, size, mass, CT pattern, shape, lobulation, spiculation, air bronchogram; between groups b and c and between a and c for vascular change and pleural indentation; and between groups a and c for sex and vacuole sign. [d], MIA and IAC are statistically significant; [e], AIS and IAC are statistically significant; [f], each pairwise comparisons are statistically significant. CT, computed tomography; AIS, adenocarcinoma in situ; MIA, minimally invasive adenocarcinoma; IAC, invasive adenocarcinoma.

Discussion

In this study, we evaluated the ability of AI-measured nodule mass to distinguish the different subtypes of neoplastic GGNs. Overall, its efficacy in differentiating was better than that of size and significantly better than that of other CT features. The optimal cutoff values of nodule mass for distinguishing between ILs and AISs and between IACs and AISs/MIAs were 225.25 mg [area under the curve (AUC) =0.821] and 390.4 mg (AUC =0.883), respectively. This indicates that the nodule mass based on AI was a reliable indicator for evaluating the invasiveness of neoplastic GGNs.

Morphological features are useful for assessing the invasiveness of neoplastic GGNs. Previous reports have highlighted a correlation of lobulation, spiculation, air cavity, air bronchogram, pleural indentation sign, and blood vessel sign with invasive GGNs (22,24). The greater

Table 2 Performance of different clinical and CT features in distinguishing ILs from AISs

Clinical and CT features	Neoplastic GGNs (AIS *vs.* ILs)				P value*
	AUC (95% CI)	P value	Sensitivity (%)	Specificity (%)	
Sex (male)	0.546 (0.510–0.581)	0.0053	31.57	77.61	<0.0001
Year (>50 years)	0.627 (0.592–0.661)	<0.0001	71.46	48.26	<0.0001
Shape (irregular)	0.637 (0.603–0.671)	<0.0001	51.42	76.06	<0.0001
Size (>9.95 mm)	0.810 (0.781–0.837)	<0.0001	64.27	84.94	0.2162
Boundary (well-defined)	0.501 (0.465–0.536)	0.935	92.06	8.11	<0.0001
Lobulation	0.610 (0.575–0.630)	<0.0001	29.68	92.28	<0.0001
Spiculation	0.595 (0.560–0.630)	<0.0001	22.87	96.14	<0.0001
Vacuole	0.529 (0.494–0.565)	0.0084	13.61	92.28	<0.0001
Air bronchial	0.592 (0.557–0.627)	<0.0001	23.44	94.98	<0.0001
Vessel change	0.521 (0.486–0.557)	0.0263	9.64	94.59	<0.0001
Pleura indentation	0.557 (0.521–0.592)	<0.0001	17.96	93.44	<0.0001
Mass (>225.25 mg)	0.821 (0.792–0.847)	<0.0001	64.27	89.19	–

*, P value of the Delong test in comparing the predictive performance of mass with that of other clinical and CT features. CT, computed tomography; IL, invasive lesion (MIAs and IACs); AIS, adenocarcinoma in situ; GGN, ground-glass nodule; AUC, area under the curve; CI, confidence interval; MIA, minimally invasive adenocarcinoma; IAC, invasive adenocarcinoma.

Table 3 Performance of different clinical and CT features in distinguishing IACs from AISs and MIAs

Clinical and CT features	Neoplastic GGNs (AIS/MIA *vs.* IAC)				P value*
	AUC (95% CI)	P value	Sensitivity (%)	Specificity (%)	
Sex (male)	0.546 (0.510–0.581)	0.0106	34.82	74.31	<0.0001
Year (>52 years)	0.628 (0.593–0.662)	<0.0001	74.09	46.58	<0.0001
Shape (irregular)	0.654 (0.620–0.687)	<0.0001	63.56	67.28	<0.0001
Size (>10.9 mm)	0.866 (0.840–0.889)	<0.0001	83.4	78.19	0.0402
Boundary (ill-defined)	0.507 (0.471–0.542)	0.5355	8.91	92.42	<0.0001
Lobulation	0.643 (0.575–0.630)	<0.0001	42.11	86.51	<0.0001
Spiculation	0.630 (0.595–0.663)	<0.0001	34.41	91.5	<0.0001
Vacuole	0.536 (0.500–0.571)	0.0076	16.6	90.57	<0.0001
Air bronchial	0.636 (0.601–0.669)	<0.0001	36.03	91.13	<0.0001
Vessel change	0.537 (0.502–0.572)	0.0019	13.36	94.09	<0.0001
Pleura indentation	0.582 (0.547–0.617)	<0.0001	25.51	90.94	<0.0001
Mass (>390.4 mg)	0.883 (0.858–0.904)	<0.0001	80.57	86.32	–

*, P value of the Delong test in comparing the predictive performance of mass with that of other clinical and CT features. CT, computed tomography; IAC, invasive adenocarcinoma; AIS, adenocarcinoma in situ; MIA, minimally invasive adenocarcinoma; GGN, ground-glass nodule; AUC, area under the curve; CI, confidence interval.

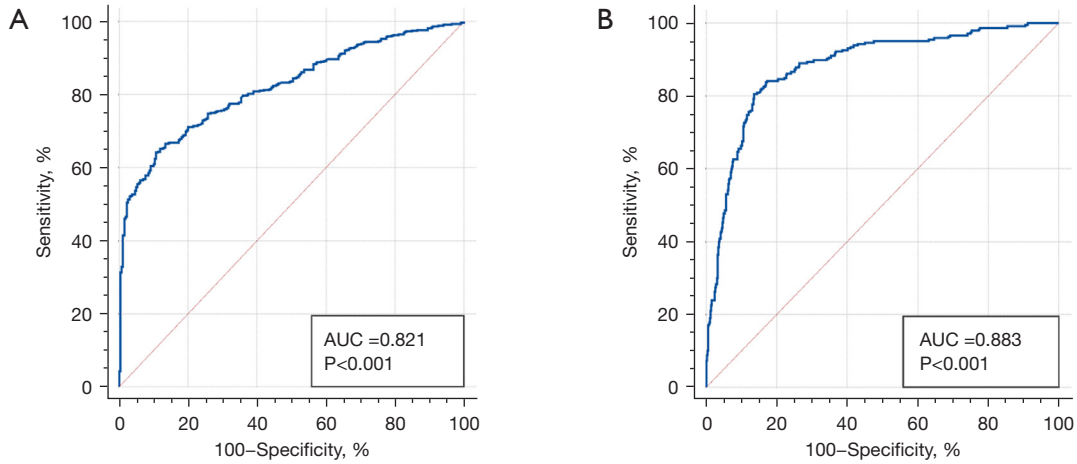

Figure 3 Receiver operating characteristic curve of nodule mass in predicting (A) ILs and (B) IACs. AUC, area under the curve; IL, invasive lesion; IAC, invasive adenocarcinoma.

Table 4 The cutoff value of nodule mass in detecting ILs (MIAs and IACs) in different lung lobes

Nodule location	Nodule mass (mg)	Sensitivity	Specificity	AUC (95% CI)	P value
Right upper lobe	203.12	0.695	0.867	0.831 (0.783–0.879)	<0.001
Left upper lobe	167.78	0.749	0.843	0.831 (0.781–0.882)	<0.001
Right lower lobe	217.21	0.692	0.897	0.838 (0.768–0.908)	<0.001
Left lower lobe	114.68	0.8	0.606	0.777 (0.686–0.868)	<0.001
Upper lobes	229.165	0.66	0.908	0.832 (0.797–0.866)	<0.001
Lower lobes	217.215	0.642	0.847	0.809 (0.753–0.865)	<0.001
Total	225.25	0.643	0.892	0.821 (0.792–0.847)	<0.001

IL, invasive lesion; MIA, minimally invasive adenocarcinoma; IAC, invasive adenocarcinoma; AUC, area under the curve; CI, confidence interval.

Table 5 The cutoff value of nodule mass in detecting IACs in different lung lobes

Nodule location	Nodule mass (mg)	Sensitivity	Specificity	AUC (95% CI)	P value
Right upper lobe	325.80	0.863	0.832	0.889 (0.847–0.932)	<0.001
Left upper lobe	365.50	0.874	0.883	0.918 (0.881–0.956)	<0.001
Right lower lobe	335.18	0.853	0.843	0.877 (0.809–0.946)	<0.001
Left lower lobe	390.65	0.727	0.871	0.84 (0.751–0.929)	<0.001
Upper lobes	325.955	0.868	0.844	0.905 (0.877–0.933)	<0.001
Lower lobes	335.18	0.806	0.824	0.858 (0.802–0.914)	<0.001
Total	390.4	0.806	0.863	0.883 (0.858–0.904)	<0.001

IAC, invasive adenocarcinoma; AUC, area under the curve; CI, confidence interval.

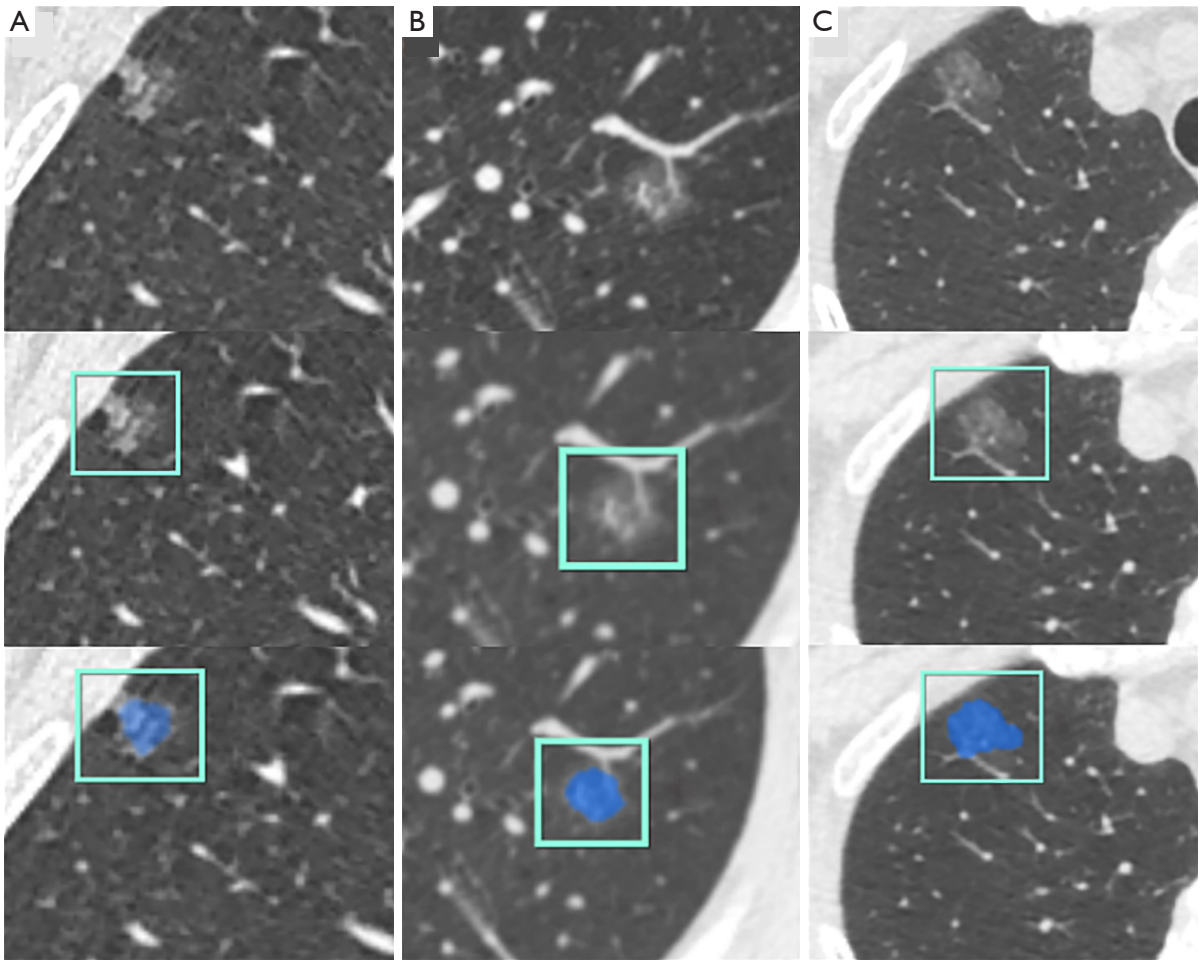

Figure 4 CT images of malignant GGNs which were similar in size but significantly different in mass. An artificial intelligence-assisted diagnosis system was used to automatically recognize and segment the GGNs from CT images and subsequently measure the nodule mass. (A) A 59-year-old woman with AIS. A transverse thin-section CT image showed an irregular and ill-defined PSN located in the right upper lobe with a size of 11 mm × 10 mm and a mass of 120.19 mg. (B) A 70-year-old man with MIA. A transverse thin-section CT image showed a round and ill-defined PSN located in the left upper lobe with a size of 11 mm × 11 mm and a mass of 295.11 mg. (C) A 59-year-old woman with IAC. A transverse thin-section CT image showed an irregular and ill-defined pGGN located in the right upper lobe with a size of 11 mm × 10 mm and a mass of 629.55 mg. CT, computed tomography; GGN, ground-glass nodule; AIS, adenocarcinoma in situ; PSN, part-solid nodule; MIA, minimally invasive adenocarcinoma; IAC, invasive adenocarcinoma; pGGN, pure ground-glass nodule.

the number of these signs present in GGNs, the higher likelihood is that they are being invasive lesions (ILs). Although the findings in this study were consistent with previous reports (16,24), the sensitivity in distinguishing GGNs was generally low because most of these features were less common in GGNs than in solid nodules. Additionally, differences in radiologists' interpretation of these signs might have introduced subjective bias. Therefore, using CT features alone to predict ILs or IACs may not be optimal.

Nodule size is an important quantitative indicator for determining the invasiveness of GGNs. The larger diameter of a nodule is, the higher likelihood of it being an IL (25). Previous research suggests that the optimal cutoff value of size in all GGNs for distinguishing MIA from AIS and atypical adenomatous hyperplasia (AAH) is 7.50 mm, that for distinguishing IAC from MIA is 12.50 mm (26), and that for distinguishing IACs from AAHs/AISs/MIAs is 10.09 mm in pGGNs (27) and 12.55 and 14.4 mm in all GGNs, respectively (28,29). Our results are similar to those

of previous studies, but there are significant differences in cutoff values, which may be due to the heterogeneity in samples from the different studies.

Besides nodule size, the density can also be used for assessing the invasiveness of neoplastic GGNs (30). A higher CT attenuation and emergence or development of solid components are all indicators of invasiveness (31,32). Reported cutoff values of mean CT attenuation in predicting the invasiveness of GGNs are –484, –495.7, and –515.95 HU (5,28,29). Additionally, the presence (>5 mm) and the new emergence or development (≥2 mm) of solid component in GGNs have been shown to be predictors of invasiveness (33). Although density and solid components are related to ILs and IACs, the heterogeneity of GGNs in density and the difficulty in accurately measuring the size of solid components can limit their value in distinguishing between GGN types (28).

The nodule mass as a parameter that combines size and density for characterizing nodules has been identified as an earlier and more stable and accurate indicator compared to other parameters (5). Nodule mass has been shown to be a superior indicator for assessing invasiveness as compared to parameters such as diameter, density, and volume (13). However, despite its reliability, nodule mass measurement is typically performed manually, which can be time-consuming and lack consistency. In recent years, AI has been increasingly used in the detection and evaluation of pulmonary nodules. AI-based semisegmentation and autosegmentation methods have proven to be rapid, accurate, and less variable compared to assessments made by experienced pathologists. However, the use of AI-derived nodule mass for evaluating the invasiveness of GGNs has not been thoroughly validated. In our study, nodule mass as measured by AI performed best in distinguishing ILs and IACs among all the parameters. This supports the potential of AI-driven nodule mass measurements in improving the assessment of GGN invasiveness. Further studies are needed to validate these findings and determine the full potential of AI in this context. However, in clinical practice, correctly evaluating the invasiveness of neoplastic GGNs cannot rely solely on the nodule mass, and it is best to conduct a comprehensive evaluation combining nodule mass and other morphological features.

In addition to automatic measurement, AI can also recognize and learn abstract high-level features that reflect the intrinsic characteristics of GGNs that are invisible to the human eye. AI modalities such as fusion mode and the image-based DL models can help radiologists differentiate between benign and malignant lesions and to identify organizing pneumonia, focal fibrosis, focal pneumonia, etc. (34,35). AI-based vessel suppression in LDCT can improve the detection of subsolid nodules and their classification into GGNs and PSNs (36). The image-based deep learning transfer learning (IBDL-TL) model can also effectively distinguish between benign and malignant GGNs (37). Meanwhile, deep CNNs and ML can distinguish different pathological subtypes of lung adenocarcinoma appearing as GGNs and identify mutations in specific genes, such as epidermal growth factor receptor (*EGFR*) mutations (38,39). Additionally, AI has been used in lung cancer staging, prognostic assessment of GGN-type lung adenocarcinoma, and detecting lung adenocarcinoma cells in pleural fluid, among other contexts (40,41).

Certain limitations to this study should be acknowledged. First, all the data were obtained from devices of the same brand of CT scanner, and thus the results may lack robustness. The results should be verified by using data from different devices. Second, we did not assess density in discriminating neoplastic GGNs with varying degrees of invasiveness due to the inconsistent diagnostic efficacy reported across different studies, with nodule size being considered as a more reliable and superior parameter than mean density. Third, the large vessels in lesions were also considered as being within the mass of nodules because they could not be completely separated, which might have affected the analysis of the mass results. Finally, the diagnostic performance of AI-based nodule mass requires further validation through the use of external, large-scale datasets.

Conclusions

For neoplastic GGNs, AI-measured nodule mass based demonstrated superior diagnostic performance in distinguishing ILs and IACs compared to other CT features. The optimal cutoff values for mass in distinguishing ILs and IACs were 225.25 and 390.4 mg, respectively. Being an easily acquired and objective indicator, AI-measured nodule mass has the potential to play a crucial role in accurately evaluating the invasiveness of neoplastic GGNs and providing information for directing further treatment.

Acknowledgments

Funding: This study received funding from the Joint Project of Chongqing Science and Technology Commission

and Chongqing Public Health Commission (No. 2022MSXM050) and the Senior Medical Talents Program of Chongqing from the Chongqing Health Commission (grant to Z.G.C.).

Footnote

Reporting Checklist: The authors have completed the STARD reporting checklist. Available at https://qims.amegroups.com/article/view/10.21037/qims-24-665/rc

Conflicts of Interest: All authors have completed the ICMJE uniform disclosure form (available at https://qims.amegroups.com/article/view/10.21037/qims-24-665/coif). The authors have no conflicts of interest to declare.

Ethical Statement: The authors are accountable for all aspects of the work in ensuring that questions related to the accuracy or integrity of any part of the work are appropriately investigated and resolved. This study was conducted in accordance with the Declaration of Helsinki (as revised in 2013) and approved by the Ethics Committee of The First Affiliated Hospital of Chongqing Medical University (No. 2019-062). The requirement for individual consent was waived due to the retrospective nature of the analysis.

References

1. Lin RY, Lv ZM, Lv FJ, Fu BJ, Liang ZR, Chu ZG. Quantitative evaluation of density variability in the lesion-lung boundary zone to differentiate pulmonary subsolid nodules. Quant Imaging Med Surg 2023;13:776-86.
2. Yan B, Chang Y, Jiang Y, Liu Y, Yuan J, Li R. A predictive model based on ground glass nodule features via high-resolution CT for identifying invasiveness of lung adenocarcinoma. Front Surg 2022;9:973523.
3. He W, Guo G, Du X, Guo S, Zhuang X. CT imaging indications correlate with the degree of lung adenocarcinoma infiltration. Front Oncol 2023;13:1108758.
4. Liang ZR, Lv FJ, Fu BJ, Lin RY, Li WJ, Chu ZG. Reticulation Sign on Thin-Section CT: Utility for Predicting Invasiveness of Pure Ground-Glass Nodules. AJR Am J Roentgenol 2023;221:69-78.
5. He S, Chen C, Wang Z, Yu X, Liu S, Huang Z, Chen C, Liang Z, Chen C. The use of the mean computed-tomography value to predict the invasiveness of ground-glass nodules: A meta-analysis. Asian J Surg 2023;46:677-82.
6. Guo CR, Xu L, Li X, Fu YL, Wang H, Han R, Li GS, Feng Z, Li M, Ren WG, Peng ZM. Computed tomography imaging and clinical characteristics of pulmonary ground-glass nodules ≤2 cm with micropapillary pattern. Thorac Cancer 2023;14:3433-44.
7. Gao J, Qi Q, Li H, Yu J, Zhang J, Lin B, Li X, Hong N, Li Y. Prediction of Lymph Node Metastasis of Mixed Ground-glass Nodules Based on Clinical Imaging Information. Zhongguo Fei Ai Za Zhi 2023;26:113-8.
8. Yang Y, Xu J, Wang W, Zhao J, Yang Y, Wang B, Ye L. Meta-analysis of the correlation between CT-based features and invasive properties of pure ground-glass nodules. Asian J Surg 2023;46:3405-16.
9. He Y, Xiong Z, Zhang J, Xie J, Zhu W, Zhao M, Li Z. Growth assessment of pure ground-glass nodules on CT: comparison of density and size measurement methods. J Cancer Res Clin Oncol 2023;149:9937-46.
10. Park J, Doo KW, Sung YE, Jung JI, Chang S. Computed Tomography Findings for Predicting Invasiveness of Lung Adenocarcinomas Manifesting as Pure Ground-Glass Nodules. Can Assoc Radiol J 2023;74:137-46.
11. Jiang J, Lv ZM, Lv FJ, Fu BJ, Liang ZR, Chu ZG. Clinical and Computed Tomography Characteristics of Solitary Pulmonary Nodules Caused by Fungi: A Comparative Study. Infect Drug Resist 2022;15:6019-28.
12. de Hoop B, Gietema H, van de Vorst S, Murphy K, van Klaveren RJ, Prokop M. Pulmonary ground-glass nodules: increase in mass as an early indicator of growth. Radiology 2010;255:199-206.
13. Qi L, Lu W, Yang L, Tang W, Zhao S, Huang Y, Wu N, Wang J. Qualitative and quantitative imaging features of pulmonary subsolid nodules: differentiating invasive adenocarcinoma from minimally invasive adenocarcinoma and preinvasive lesions. J Thorac Dis 2019;11:4835-46.
14. He Y, Xiong Z, Tian D, Zhang J, Chen J, Li Z. Natural progression of persistent pure ground-glass nodules 10 mm or smaller: long-term observation and risk factor

assessment. Jpn J Radiol 2023;41:605-16.
15. Youguo Z, Chengye W, Xiaofei C, Xuefei Z, Changhong L. Analysis of the relevance between computed tomography characterization and pathology of pulmonary ground-glass nodules with different pathology types. Turk Gogus Kalp Damar Cerrahisi Derg 2023;31:95-104.
16. Quanyang W, Yao H, Sicong W, Linlin Q, Zewei Z, Donghui H, Hongjia L, Shijun Z. Artificial intelligence in lung cancer screening: Detection, classification, prediction, and prognosis. Cancer Med 2024;13:e7140.
17. Tang TW, Lin WY, Liang JD, Li KM. Artificial intelligence aided diagnosis of pulmonary nodules segmentation and feature extraction. Clin Radiol 2023;78:437-43.
18. Chassagnon G, De Margerie-Mellon C, Vakalopoulou M, Marini R, Hoang-Thi TN, Revel MP, Soyer P. Artificial intelligence in lung cancer: current applications and perspectives. Jpn J Radiol 2023;41:235-44.
19. de Margerie-Mellon C, Chassagnon G. Artificial intelligence: A critical review of applications for lung nodule and lung cancer. Diagn Interv Imaging 2023;104:11-7.
20. Liu L, Ni Z, Zhang J, Zhao J, Shen J. Application of artificial intelligence-based dual source CT scanning in the differentiation of lung adenocarcinoma in situ and minimally invasive adenocarcinoma. Pak J Med Sci 2024;40:271-6.
21. Fu G, Yu H, Liu J, Xia T, Xiang L, Li P, Huang D, Lin L, Zhuang Y, Yang Y. Arc concave sign on thin-section computed tomography: A novel predictor for invasive pulmonary adenocarcinoma in pure ground-glass nodules. Eur J Radiol 2021;139:109683.
22. Hsu WC, Huang PC, Pan KT, Chuang WY, Wu CY, Wong HF, Yang CT, Wan YL. Predictors of Invasive Adenocarcinomas among Pure Ground-Glass Nodules Less Than 2 cm in Diameter. Cancers (Basel) 2021;13:3945.
23. Gao J, Qi Q, Li H, Wang Z, Sun Z, Cheng S, Yu J, Zeng Y, Hong N, Wang D, Wang H, Yang F, Li X, Li Y. Artificial-intelligence-based computed tomography histogram analysis predicting tumor invasiveness of lung adenocarcinomas manifesting as radiological part-solid nodules. Front Oncol 2023;13:1096453.
24. Cai Y, Chen T, Zhang S, Tan M, Wang J. Correlation exploration among CT imaging, pathology and genotype of pulmonary ground-glass opacity. J Cell Mol Med 2023;27:2021-31.
25. Yang HH, Lv YL, Fan XH, Ai ZY, Xu XC, Ye B, Hu DZ. Factors distinguishing invasive from pre-invasive adenocarcinoma presenting as pure ground glass pulmonary nodules. Radiat Oncol 2020;15:186.
26. Shi Y, Shen Y, Chen J, Yan W, Liu K. Value of CT Quantitative Parameters in Prediction of Pathological Types of Lung Ground Glass Nodules. Zhongguo Fei Ai Za Zhi 2024;27:118-25.
27. Sun Y, Li C, Jin L, Gao P, Zhao W, Ma W, Tan M, Wu W, Duan S, Shan Y, Li M. Radiomics for lung adenocarcinoma manifesting as pure ground-glass nodules: invasive prediction. Eur Radiol 2020;30:3650-9.
28. Wang H, Yang H, Liu Z, Chen L, Xu X, Zhu Q. Comparison of Two-dimensional and Three-dimensional Features of Chest CT in the Diagnosis of Invasion of Pulmonary Ground Glass Nodules. Zhongguo Fei Ai Za Zhi 2022;25:723-9.
29. Zhou Y, Zhang Y, Zhang S, Zhang C, Chen Z. Growth Regularity of Pulmonary Ground Glass Nodules Based on 3D Reconstruction Technology. Zhongguo Fei Ai Za Zhi 2023;26:265-73.
30. Youguo Z, Chengye W, Xiaofei C, Xuefei Z, Changhong L. Analysis of the relevance between computed tomography characterization and pathology of pulmonary ground-glass nodules with different pathology types. Turk Gogus Kalp Damar Cerrahisi Derg 2023;31:95-104.
31. Tao G, Zhu L, Chen Q, Yin L, Li Y, Yang J, Ni B, Zhang Z, Koo CW, Patil PD, Chen Y, Yu H, Xu Y, Ye X. Prediction of future imagery of lung nodule as growth modeling with follow-up computed tomography scans using deep learning: a retrospective cohort study. Transl Lung Cancer Res 2022;11:250-62.
32. Zhang H, Wang D, Li W, Tian Z, Ma L, Guo J, Wang Y, Sun X, Ma X, Ma L, Zhu L. Artificial intelligence system-based histogram analysis of computed tomography features to predict tumor invasiveness of ground-glass nodules. Quant Imaging Med Surg 2023;13:5783-95.
33. Wang Z, Zhu W, Lu Z, Li W, Shi J. Invasive adenocarcinoma manifesting as pure ground glass nodule with different size: radiological characteristics differ while prognosis remains the same. Transl Cancer Res 2021;10:2755-66.
34. Huang W, Deng H, Li Z, Xiong Z, Zhou T, Ge Y, Zhang J, Jing W, Geng Y, Wang X, Tu W, Dong P, Liu S, Fan L. Baseline whole-lung CT features deriving from deep learning and radiomics: prediction of benign and malignant pulmonary ground-glass nodules. Front Oncol 2023;13:1255007.
35. Qiu Z, Wu Q, Wang S, Chen Z, Lin F, Zhou Y, Jin J, Xian

J, Tian J, Li W. Development of a deep learning-based method to diagnose pulmonary ground-glass nodules by sequential computed tomography imaging. Thorac Cancer 2022;13:602-12.
36. Singh R, Kalra MK, Homayounieh F, Nitiwarangkul C, McDermott S, Little BP, Lennes IT, Shepard JO, Digumarthy SR. Artificial intelligence-based vessel suppression for detection of sub-solid nodules in lung cancer screening computed tomography. Quant Imaging Med Surg 2021;11:1134-43.
37. Wang X, Gao M, Xie J, Deng Y, Tu W, Yang H, Liang S, Xu P, Zhang M, Lu Y, Fu C, Li Q, Fan L, Liu S. Development, Validation, and Comparison of Image-Based, Clinical Feature-Based and Fusion Artificial Intelligence Diagnostic Models in Differentiating Benign and Malignant Pulmonary Ground-Glass Nodules. Front Oncol 2022;12:892890.
38. O'Sullivan DE, Jarada TN, Yusuf A, Hu LXY, Gogna P, Brenner DR, Abbie E, Rose JB, Eaton K, Elia-Pacitti J, Ewara EM, Pabani A, Cheung WY, Boyne DJ. Prevalence, Treatment Patterns, and Outcomes of Individuals with EGFR Positive Metastatic Non-Small Cell Lung Cancer in a Canadian Real-World Setting: A Comparison of Exon 19 Deletion, L858R, and Exon 20 Insertion EGFR Mutation Carriers. Curr Oncol 2022;29:7198-208.
39. Venugopalan A, Lynberg M, Cultraro CM, Nguyen KDP, Zhang X, Waris M, Dayal N, Abebe A, Maity TK, Guha U. SCAMP3 is a mutant EGFR phosphorylation target and a tumor suppressor in lung adenocarcinoma. Oncogene 2021;40:3331-46.
40. Fang W, Zhang G, Yu Y, Chen H, Liu H. Identification of pathological subtypes of early lung adenocarcinoma based on artificial intelligence parameters and CT signs. Biosci Rep 2022;42:BSR20212416.
41. Liu W, Shen N, Zhang L, Wang X, Chen B, Liu Z, Yang C. Research in the application of artificial intelligence to lung cancer diagnosis. Front Med (Lausanne) 2024;11:1343485.

Cite this article as: Xiong TW, Gan H, Lv FJ, Zhang XC, Fu BJ, Chu ZG. Artificial intelligence-measured nodule mass for determining the invasiveness of neoplastic ground glass nodules. Quant Imaging Med Surg 2024;14(9):6698-6710. doi: 10.21037/qims-24-665

